

A computational study of high-speed microdroplet impact onto a smooth solid surface

James Q. Feng

Optomec, Inc., 2575 University Avenue, Suite 135, St. Paul, Minnesota 55114, USA

E-mail: jfeng@optomec.com

Abstract. Numerical solutions of high-speed microdroplet impact onto a smooth solid surface are computed, using the *interFoam* VoF solver of the OpenFOAM[®] CFD package. Toward the solid surface, the liquid microdroplet is moving with an impinging gas flow, simulating the situation of ink droplets being deposited onto substrate with a collimated mist jet in the Optomec Aerosol Jet[®] printing process. For simplicity and computational efficiency, axisymmetric incompressible flow is assumed in the present study of the free-surface fluid dynamic problem. The computed values of maximum spread factor, for the range of parameters of practical interest to Aerosol Jet[®] printing, were found in very good agreement with some of the correlation formulas proposed by previous authors in the literature. Combining formulas selected from different authors with appropriate modifications yields a maximum spread factor formula that can be used for first-order evaluations of deposited droplet size during the Aerosol Jet[®] technology development. The computational results also illustrate droplet impact dynamics with lamella shape evolution throughout the spreading, receding-relaxation, and wetting equilibrium phases, consistent with that observed and described by many previous authors. This suggests a scale-invariant nature of the basic droplet impact behavior such that experiments with larger droplets at the same nondimensional parameter values may be considered for studying microdroplet impact dynamics. Significant free surface oscillations can be observed when the droplet viscosity is relatively low. The border line between periodic free surface oscillations and aperiodic creeping to capillary equilibrium free surface shape appears at the value of Ohnesorge number around 0.25. Droplet bouncing after receding is prompted with large contact angles at solid surface (as consistent with findings reported in the literature), but can be suppressed by increasing the droplet viscosity.

Keywords: Drop impact, Microdroplet, Aerosol Jet[®], Volume-of-fluid (VoF), Computational analysis

1. Introduction

With the Aerosol Jet[®] direct-write technology, ink microdroplets generated by a liquid atomization process are deposited onto a substrate in a form of collimated mist stream (which can become less than $10\ \mu\text{m}$ in diameter having the ink droplet concentration typically about $50\ \text{nL/cc}$) with considerable impinging velocity, e.g., 20 to 100 m/s (cf. Renn, 2006; Zollmer et al., 2006; Renn, 2007; Hedges et al., 2007; Kahn, 2007; Renn et al., 2009, 2010; Christenson et al., 2011; Paulsen et al., 2012). Therefore, the ink droplets can have sufficient momentum to impact the substrate several millimeters away from the deposition nozzle as directed by the high-speed jet flow (cf. Feng, 2015). The Aerosol Jet[®] functional inks typically consist of suspensions of nano-particles or polymer solutions formulated with appropriate properties such that they can be adequately aerosolized with a liquid atomizer. The ink droplet diameter is usually in a narrow range of 1 to $5\ \mu\text{m}$ with the volume mean diameter around $2.5\ \mu\text{m}$, such that fine features as small as $\sim 10\ \mu\text{m}$ can be produced by the additive manufacturing process. As with many industrial applications such as spray coating, inkjet printing, and so forth, understanding of droplet deposition behavior is important for achieving desired Aerosol Jet[®] print quality. Therefore, a detailed analysis of high-speed microdroplet impact on a solid surface can provide practically valuable insights.

The process of droplet impact on a surface involves a rich set of free-surface fluid dynamics phenomena, ranging from spreading, receding, oscillating, to bouncing, splashing, etc. (Yarin, 2006). It has been a subject of intensive study by many authors (e.g., Ford and Furnidge, 1967; Foote, 1974; Chandra and Avedisian, 1991; Rein, 1993; Healy et al., 1996; Bussmann et al., 1999, 2000; Sikalo et al., 2002; Rioboo et al., 2001, 2002; Toivakka, 2003; Law, 2015, as well as references cited therein), for its relevance to a wide variety of applications. Yet, our understanding of the associated fluid dynamics may still be far from thorough, probably due to the difficulties in consistent characterizations of wetting and surface properties as well as lack of agreeable formulations of moving contact line boundary conditions for theoretical modeling. For example, numerous empirical and semi-empirical formulas were proposed for describing the maximum spread factor, defined as the maximum normalized contact diameter of the lamella at the end of spreading phase, for its practical importance (e.g., Scheller and Bousfield, 1995; Pasandideh-Fard et al., 1996; Toivakka, 2003; Attane et al., 2007; Roisman, 2009; German and Bertola, 2009); each has an apparently different form and quantitative agreement with each other for a given case usually does not seem as good as one would hope (cf. Perelaer et al., 2009; Ravi et al., 2010; Visser et al., 2012, 2015). This makes it very difficult to decide which formula to use for estimating the spot size as a result of each ink droplet impact on the substrate with parameters of particular interest.

Because the Aerosol Jet[®] printing process involves micron-size droplets carried by a high-speed impinging gas jet at velocity typically around 50 m/s, experimental investigations can be quite challenging and prohibitively expensive, if not impossible. Rather recently Visser et al. (2012, 2015) have reported experimental measurements of microdroplet impact with an interferometric technique that enabled sub-micron spatial resolution at frame rates exceeding

10^7 per second, which still seems to be an order of magnitude short for the Aerosol Jet[®] situation. To date, computational analysis with numerical solutions of the governing equations may be the only option for gaining insights into the micron-size droplet impact at high velocity relevant to the Aerosol Jet[®] additive manufacturing process.

Due to extensive free surface deformations involved in droplet impact process, numerical computations have remained challenging. Although the explicit interface tracking method with boundary-fitted moving mesh using an arbitrary Lagrangian-Eulerian scheme offers the highest accuracy for the free-surface flow problem, it is mostly effective for the types of problems with moderate free surface deformations without topology changes (e.g., Feng, 2010, 2015) and becomes too complicated to be practically applicable to the situation of droplet impact problem where phase topology can change with significant free surface movement or even disintegration. On the other hand, the implicit Eulerian interface capturing methods such as volume of fluid (VoF) have been developed for effective computations of flows involving substantial topology changes with interface breaking (because the mesh does not need to move with the interface), despite some compromise of numerical accuracy. Among many versions of the VoF solvers, the *interFoam* of an open-source CFD package called OpenFOAM[®] has been attractive to numerous users and validated by many authors (Berberovic et al., 2009; Saha and Mitra, 2009; Deshpande et al., 2012; Morgan, 2013; Hoang et al., 2013). Over years of code development and testing, the numerical algorithms implemented in *interFoam* have been continuously improved to enable reasonably accurate interface representation with effective advection treatment, handling large density ratios, reducing “spurious (parasitic) currents”, and so forth (Gopala and van Wachem, 2008; Deshpande et al., 2012).

The purpose of the present work is to compute axisymmetric solutions of a droplet impact on a solid surface with parameters relevant to the Aerosol Jet[®] printing, using the well-established *interFoam* VoF solver. Through detailed comparisons of the computed results with the available formulas from different authors, a reliable correlation formula for the maximum spread factor can be obtained for predicting the deposition spot size on substrate corresponding to a single ink droplet impact. Such spot sizes directly relate to achievable resolutions with the ink droplet size distribution involved in the Aerosol Jet[®] additive manufacturing process. Moreover, the numerical solutions can also reveal other possible outcomes beyond spreading phase, such as oscillations, bouncing, etc. In what follows, a brief description of the problem formulation and computational method is presented in section 2, the numerical results for Weber number $We = 2500, 100, \text{ and } 5$ are presented in section 3 with discussion of implications for Aerosol Jet[®] printing given in section 4, and concluding remarks are provided in section 5.

2. Problem statement and computational method

Considered here is a liquid droplet of density ρ_d , viscosity μ_d , surface tension σ , and diameter d impacting a smooth solid surface as carried by a gas impinging flow at velocity U (figure 1). The surrounding gas has density ρ_g and viscosity μ_g . Solutions to the Navier-Stokes

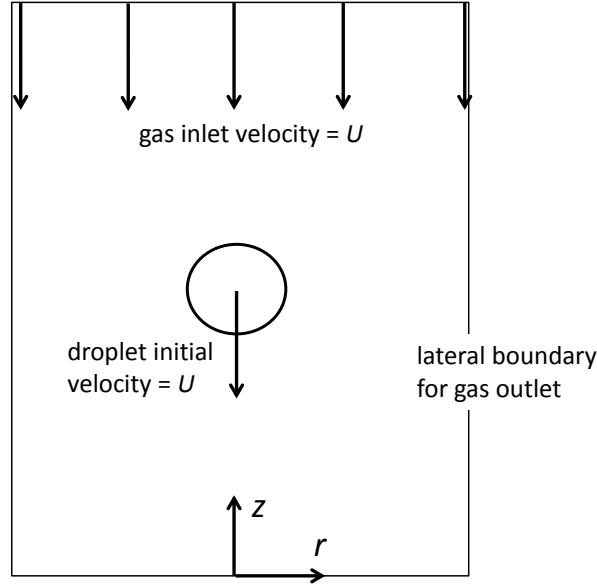


Figure 1. Schematics of a droplet moving with impinging gas flow at velocity U to impact a solid surface.

equations for incompressible Newtonian fluids are computed using the *interFoam* VoF solver of the OpenFOAM[®] CFD package.

With the volume-of-fluid (VoF) method, an indicator function α (also called the phase fraction function) is used to represent the volume fraction of one of the phases. The discontinuity at a gas-liquid interface is represented by a gradient of the continuous function α . Therefore, the interface is rendered as a diffuse layer with finite thickness on the order of the finite volume cell size, and the interface location may not be determined precisely with sub-grid resolution. Two immiscible fluids are treated as one effective fluid throughout the problem domain, having a continuously distributed phase fraction function α ($0 \leq \alpha \leq 1$) as well as distributed density ρ and viscosity μ according to

$$\rho \equiv \rho_d \alpha + \rho_g (1 - \alpha) \text{ and } \mu \equiv \mu_d \alpha + \mu_g (1 - \alpha) \quad . \quad (1)$$

To improve the interface resolution, the transport equation for phase fraction function used in *interFoam* is of the form (Ubbink, 2002; Rusche, 2002; Berberovic et al., 2009)

$$\frac{\partial \alpha}{\partial t} + \nabla \cdot (\alpha \mathbf{u}) + \nabla \cdot [\alpha (1 - \alpha) \mathbf{u}_r] = 0 \quad , \quad (2)$$

where the velocity of the effective fluid and relative velocity are respectively

$$\mathbf{u} \equiv \alpha \mathbf{u}_d + (1 - \alpha) \mathbf{u}_g \text{ and } \mathbf{u}_r \equiv \mathbf{u}_d - \mathbf{u}_g \quad .$$

Then, the momentum equation can be written as

$$\frac{\partial (\rho \mathbf{u})}{\partial t} + \nabla \cdot (\rho \mathbf{u} \mathbf{u}) - \nabla \cdot (\mu \nabla \mathbf{u}) - (\nabla \mathbf{u}) \cdot \nabla \mu = -\nabla p - g \mathbf{e}_g \cdot \mathbf{x} \nabla \rho + \sigma \kappa \nabla \alpha \quad , \quad (3)$$

where σ denotes the interfacial tension and κ the mean curvature of the free interface, determined from

$$\kappa \equiv -\nabla \cdot \left(\frac{\nabla \alpha}{|\nabla \alpha|} \right) . \quad (4)$$

In (3), g is the value and \mathbf{e}_g the unit vector of gravitational acceleration, \mathbf{x} is the position vector, and p the lumped (or piezometric) pressure defined as

$$p \equiv p_0 - \rho g \mathbf{e}_g \cdot \mathbf{x} ,$$

with p_0 denoting the thermodynamic pressure. For incompressible flow, the velocity field also satisfies the continuity equation

$$\nabla \cdot \mathbf{u} = 0 . \quad (5)$$

As illustrated in figure 1, no-slip boundary condition ($\mathbf{u} = \mathbf{0}$) is applied at the solid surface ($z = 0$), and a uniform-fixed-value velocity ($\mathbf{u} = -U\mathbf{e}_z$) is specified at the inlet ($z = 10 \times d$), where \mathbf{e}_z denotes the unit normal vector in z -direction. At the outlet ($r = 5 \times d$), a fixed-value pressure is specified with the “pressureInletOutletVelocity” boundary condition for flow velocity. At the three-phase contact line, the “dynamicAlphaContactAngle” condition according to

$$\theta = \theta_0 + (\theta_A - \theta_R) \tanh(u_w/u_\theta) \quad (6)$$

is used with the static contact angle θ_0 , leading edge contact angle θ_A , trailing edge contact angle θ_R , and velocity scaling u_θ being specified. The contact line moving velocity along the solid wall is denoted by u_w in (6), which becomes part of the solution when specifying the contact angle condition related to $\nabla \alpha$ at the contact line that is implicitly allowed to move (or “slip”) in the local cell (cf. Saha and Mitra, 2009; Linder et al., 2013). Without complete agreement on the boundary conditions to be implemented at the moving contact line for modeling (Yarin, 2006), the parameter values for “dynamicAlphaContactAngle” are selected somewhat arbitrarily in the present work only for demonstrating the possible fluid dynamics phenomena.

More often than not in Aerosol Jet[®] operations, the collimated mist stream is arranged to impinge perpendicularly onto the substrate. With the mist stream wrapped in a thick gas sheath and substrate typically located more than $10 \times$ the nozzle diameter away from nozzle exit, the individual ink droplets can be reasonably assumed to impact substrate perpendicularly with negligible deviations. Because the relevant droplet impact problem can be simplified to an axisymmetric configuration with a simple rectangular domain as shown in figure 1, a mesh with wedge cells is generated with the *blockMesh* utility to take advantage of axisymmetry for computations of cases in the present study. To ensure adequate resolution of the droplet free surface profile, the impaction region contains finite volume quadrilateral cells with side length less than $0.01 \times d$ (comparable to that used by Toivakka, 2003; Dinc and Gray, 2012, for VoF computations of drop impact problems). Initial position of the droplet center is set at $5 \times d$ with the droplet initial velocity set as the impinging gas jet velocity U , using the *funkySetFields* utility of “swak4foam” with OpenFOAM[®].

For the nominal setting, the surrounding gas (e.g., nitrogen—the typical mist carrier gas used in Aerosol Jet[®] process—under ambient temperature and pressure) is assumed to have $\rho_g = 1.2 \text{ kg m}^{-3}$ and $\mu_g = 1.8 \times 10^{-5} \text{ N s m}^{-2}$, whereas the liquid droplet typically have $\rho_d = 2 \times 10^3$ (but may vary between $1 \times$ and 4×10^3) kg m^{-3} and μ_d in a range between 1×10^{-3} and 1 N s m^{-2} , representing the inks used in Aerosol Jet[®] printing. The surface tension of the droplet σ is assumed to be constant with a nominal value of 0.04 (but may vary between 0.02 and 0.08) N m^{-1} .

As usual in fluid dynamics analysis, nondimensional parameters can be conveniently utilized. If ρ and μ are respectively measured in units of ρ_d and μ_d , length in units of d , velocity in units of U , time in units of d/U , and pressure in units of $\mu_d U/d$, three parameters would appear in the nondimensionalized (3) such as the Reynolds number $Re \equiv \rho_d U d / \mu_d$ in front of the first and second terms on left side, the inverse capillary number $1/Ca \equiv \sigma / (\mu_d U)$ in place of σ and $\rho_d g d^2 / (\mu_d U) \equiv Bo/Ca$ in place of g on right side, with Bo denoting the Bond number $\rho_d g d^2 / \sigma$. Because the value of Bo/Ca (as the ratio of the terminal velocity under gravity and impacting velocity U) even for a droplet of $d = 10^{-5} \text{ m}$, $\rho_d = 5 \times 10^3 \text{ kg m}^{-3}$ and $\mu_d = 10^{-3} \text{ N s m}^{-2}$ at $U = 10 \text{ m/s}$ with $g = 9.81 \text{ m s}^{-2}$ is $< 5 \times 10^{-3}$, the effect of gravity in Aerosol Jet[®] ink droplet deposition (where U is typically $> 20 \text{ m/s}$) should be rather negligible. Thus, only Reynolds number Re ($\equiv \rho_d U d / \mu_d$) and capillary number Ca ($\equiv \mu_d U / \sigma$) need to be specified as independent parameters in computing the numerical results.

3. Numerical results

Since the diameter of ink droplets rarely exceeds $5 \mu\text{m}$ in Aerosol Jet[®] printing, we start by examining cases with a droplet of $d = 5 \mu\text{m}$, $\rho_d = 2 \times 10^3 \text{ kg m}^{-3}$, $\mu_d = 10^{-3} \text{ N s m}^{-2}$ (or 1 cp). As a reference, at $U = 100 \text{ m/s}$ (which represents the high end of mist jet velocity in Aerosol Jet[®] printing) and $\sigma = 0.04 \text{ N m}^{-1}$, the value of Re and Ca are 1000 and 2.5, respectively. When studying the droplet impact problem, many authors often refer to the Weber number $We \equiv \rho_d U^2 d / \sigma = Re Ca$ and the Ohnesorge number $Oh \equiv \mu_d / \sqrt{\rho_d \sigma d} = \sqrt{Ca/Re}$ (Yarin, 2006), which will also be used here as derived dimensionless parameters in discussion. (Among Re , Ca , We , and Oh , once two of them are specified as independent parameters the other two can then be determined from those specified two.) Corresponding to $Re = 1000$ and $Ca = 2.5$, we have $We = 2500$ and $Oh = 0.05$ which represent cases of low viscosity ink drops of large sizes at high impact velocity relevant to Aerosol Jet[®] printing. In another extreme with an ink droplet of $d = 1 \mu\text{m}$, $\rho_d = 1 \times 10^3 \text{ kg m}^{-3}$, $\mu_d = 0.1 \text{ N s m}^{-2}$ (or 100 cp), the values of Re and Ca for $\sigma = 0.08 \text{ N m}^{-1}$ and impacting at $U = 20 \text{ m/s}$ become 0.2 and 25, yielding $We = 5$ and $Oh = 11.18$. Although dimensional parameter values are often referred to here, the results with plots are presented in terms of dimensionless parameters with length measured in units of d , velocity in units of U , and time t in units of d/U , for generality. The condition at contact line (6) is specified as a static contact angle θ_0 with $\theta_A = \theta_0 + 5^\circ$, $\theta_R = \theta_0 - 5^\circ$ and $u_\theta = 1 \text{ m/s}$ for *interFoam* computations.

With transient terms discretized using a first-order implicit Euler scheme, the time step is

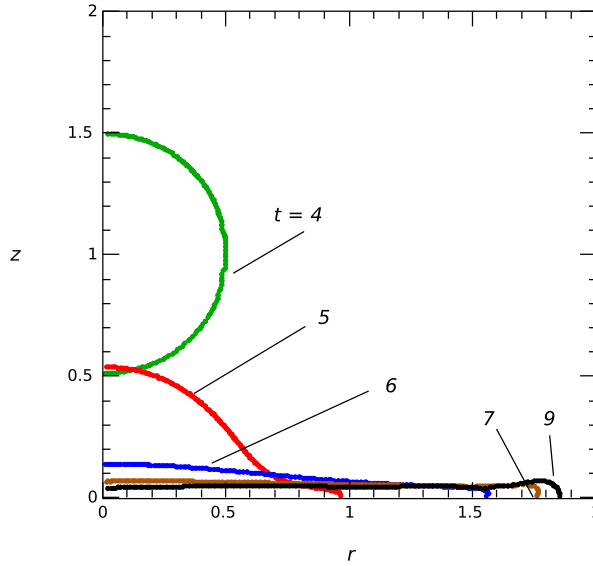


Figure 2. Spreading: shapes of a droplet of $d = 5 \mu\text{m}$, $\rho_d = 2000 \text{ kg m}^{-3}$, and $\mu_d = 1 \text{ cp}$ with $\sigma = 0.04 \text{ N m}^{-1}$, impacting solid surface at $U = 100 \text{ m/s}$ ($Re = 1000$ and $Ca = 2.5$, or $We = 2500$ and $Oh = 0.05$) with contact angle $\theta_0 = 90^\circ$ for dimensionless time $t = 4, 5, 6, 7,$ and 9 in units of $d/U (= 0.05 \mu\text{s})$, from initial dimensionless position at $z = 5$ at $t = 0$. The dimensionless coordinates r and z are labeled in units of d . The free surface profile data came from the output csv file of the *ParaView* contour for $\alpha = 0.5$.

controlled by setting the maximum Courant number to 0.01 (which is much finer than “ < 0.5 ” as recommended by many authors to avoid significant spurious currents). For postprocessing the numerical results, an open-source multi-platform data analysis package called *ParaView* (available at www.paraview.org) for scientific visualization is used in the present work.

3.1. Cases of $We = 2500$

Droplets at large We (e.g., $We = 2500$) are expected to have relatively more significant dynamical deformations and to exhibit more dramatic fluid dynamics phenomena. Shown in figure 2 are the free surface profiles of a droplet impacting a solid surface and spreading as the contact radius increases with time at $Re = 1000$ and $Ca = 2.5$, for $\theta_0 = 90^\circ$ (with $\theta_A = 95^\circ$, $\theta_R = 85^\circ$, and $u_\theta = 1 \text{ m/s}$). It appears that the droplet has little deformation before impacting the solid surface, because the value of the Weber number based on gas flow $We_g \equiv (\rho_g/\rho_d) \times Re Ca$ is only 1.5, as consistent with the findings of Feng (2010) that noticeable deformations of liquid droplet moving in a gas medium are not expected for $We_g < 5$. Soon after the droplet of 0.5 radius (in units of d) contacts the solid surface, it spreads to a maximum contact radius about 1.85 at $t \approx 9$ (in units of $d/U = 0.05 \mu\text{s}$ for $d = 5 \mu\text{m}$ and $U = 100 \text{ m/s}$). It should be noted that the center of droplet is initially located at $z = 5$ at $t = 0$ moving at dimensionless velocity 1 (in units of U toward the solid surface (at $z = 0$); therefore, the droplet bottom pole reaches the solid surface around $t = 4.5$. From $t = 4.5$ to 5, the contact line moves from $r = 0$ to $r = 1$ (as indicated in figure 2) with an estimated average speed of ~ 2 units of U . Then, the speed of contact line motion is reduced to ~ 0.6 from $t = 5$ to 6

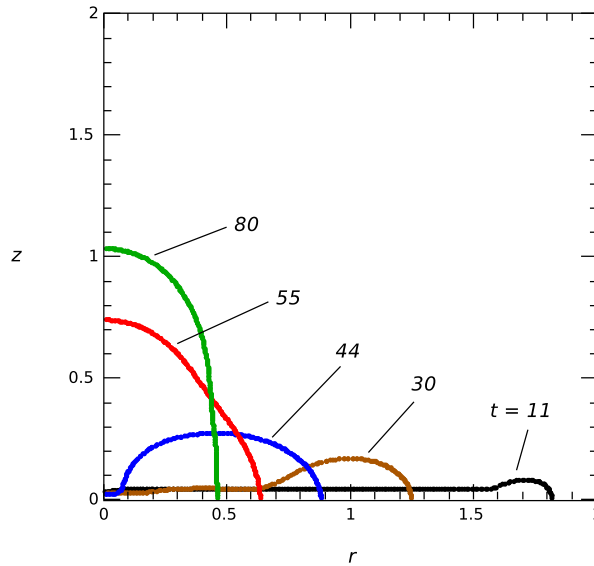


Figure 3. Receding: as in figure 2 but for $t = 11, 30, 44, 55,$ and 80 .

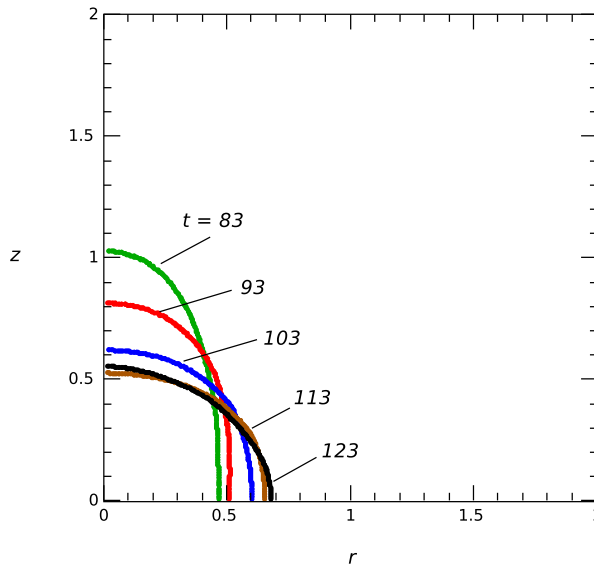


Figure 4. Oscillating: as in figure 2 but for $t = 83, 93, 103, 113,$ and 123 .

and to ~ 0.2 from $t = 6$ to 7 as the droplet becomes a lamella, and thereafter further down to 0 at $t \approx 9$. The time for spreading process, which is sometimes called the “spreading time” (e.g., Antonini et al., 2012), is $\approx 4.5 \times d/U$ ($= 0.225 \mu\text{s}$ for $d = 5 \mu\text{m}$ and $U = 100 \text{ m/s}$).

After spreading to the maximum contact radius, the lamella enters the receding (or relaxation) phase with the contact radius shrinking with time from $t \approx 9$ until $t \approx 80$, as shown in figure 3. In the receding process, a growing bulged rim forms around the contact line as it moves toward the center at an average speed of ~ 0.018 units of U , much slower than that in the spreading process. The inner edge of the bulged rim collapse at the center around $t = 44$ and thereafter the droplet center is pushed to move upward quickly. At $t = 55$, the contact line arrives the neighborhood of its equilibrium position $r \approx 0.63$. Because of

large $Re = 1000$, the contact radius continues to recede past its equilibrium position toward $r \approx 0.46$ at $t = 80$. At the same time, the upper pole of free surface reaches its maximum height of $z \approx 1.03$.

What follows the receding of contact radius is the sessile droplet oscillation up and down around its equilibrium hemispherical shape with a radius ≈ 0.63 , due to relatively strong inertial effect at $Re = 1000$. Even at $t = 103$ when the contact radius and upper pole are close to their equilibrium value (0.63), the free surface appears to still deviate noticeably from its equilibrium hemispherical shape. But the oscillation amplitude will decay quickly with time by viscous damping, which can clearly be seen in figure 5.

The center height H and contact radius R (in units of d) versus time are shown in figure 5 for droplets of $d = 5 \mu\text{m}$, $\rho_d = 2000 \text{ kg m}^{-3}$, $\sigma = 0.04 \text{ N m}^{-1}$ with $\mu_d = 1 \text{ cp}$, 2 cp , 5 , and 10 cp , impacting solid surface at $U = 100 \text{ m/s}$. For the case of $Re = 1000$ and $Ca = 2.5$ (corresponding to that shown in figures 2–4), the droplet exhibits significant oscillations after impaction. Since the initial oscillation amplitude is quite large, the waveform does not appear to be simply sinusoidal (non-sinusoidal oscillations were also shown in experimental results of Ravi et al., 2010). But the oscillation amplitude decays with time due to viscous damping. If the droplet viscosity is increased to 2 cp (at $Re = 500$ and $Ca = 5$) the amplitude of free surface oscillation diminishes rather quickly due to viscous damping after about one cycle. Oscillations do not seem to occur for $\mu_d > 5 \text{ cp}$ (for $Oh > 0.25$) indicating the deformed free surface after impaction creeps aperiodically to the equilibrium shape of a hemisphere. After impaction, the center height H appears to decrease with t monotonically when Re is large reaching its minimum value right before the bulge rim collapse at the center. For example, the values of H_{min} are 0.0266 at $t = 36$ and 0.0231 at $t = 41$ for $Re = 1000$ and 500 , respectively. But with reducing the value of Re (corresponding to increasing viscosity μ_d) the value of H_{min} tends to occur at smaller t and then slowly increase. For example, when $Re = 200$ and 100 $H_{min} = 0.0858$ at $t = 9$ and $H_{min} = 0.0998$ at $t = 9$, respectively.

Immediately after the impaction, the contact radius R (which is equivalent to one half of the so-called ‘spread factor’) increases according to a square-root law, such as $R \propto \sqrt{t^*}$ for $t^* \equiv t - t_0$ with t_0 denoting the time for the impacting droplet to initiate contact to the substrate, typically referred to as the kinematic phase when material points in the droplet mainly move in the z -direction rather than r -direction (Rioboo et al., 2002). For the cases of $We = 2500$ in figure 5, a curve fit of $R = 1.1\sqrt{t^*}$ for $t_0 = 4.51$ appears to be quite accurate for $0 \leq t^* \leq 0.15$, just as expected with the kinematic phase (usually considered for $t^* \ll 1$). As a reference, some fittings of experimental data showed $R = 1.4\sqrt{t^*}$ (Rioboo et al., 2002), yet others had $R = 0.675\sqrt{t^*}$ (e.g., Gupta and Kumar, 2010). The droplet typically takes the shape of a ‘cut sphere’ during the kinematic phase, similar to that at $t = 5$ in figure 2, until a lamella—radially expanding film bounded by a rim—forms in the spreading phase (like the profiles shown in figure 2 for $t > 6$). All curves of R versus t in figure 5 exhibit a common feature with a quick increase of R immediately after the impact at $t \sim 4.5$ until $t \sim 9$ where R reaches a peak value, and then R decreases with t at a much slower speed. The spreading phase ends when the spreading velocity approaches zero, which usually corresponds to R arriving at its peak value. Following the spreading phase the lamella may

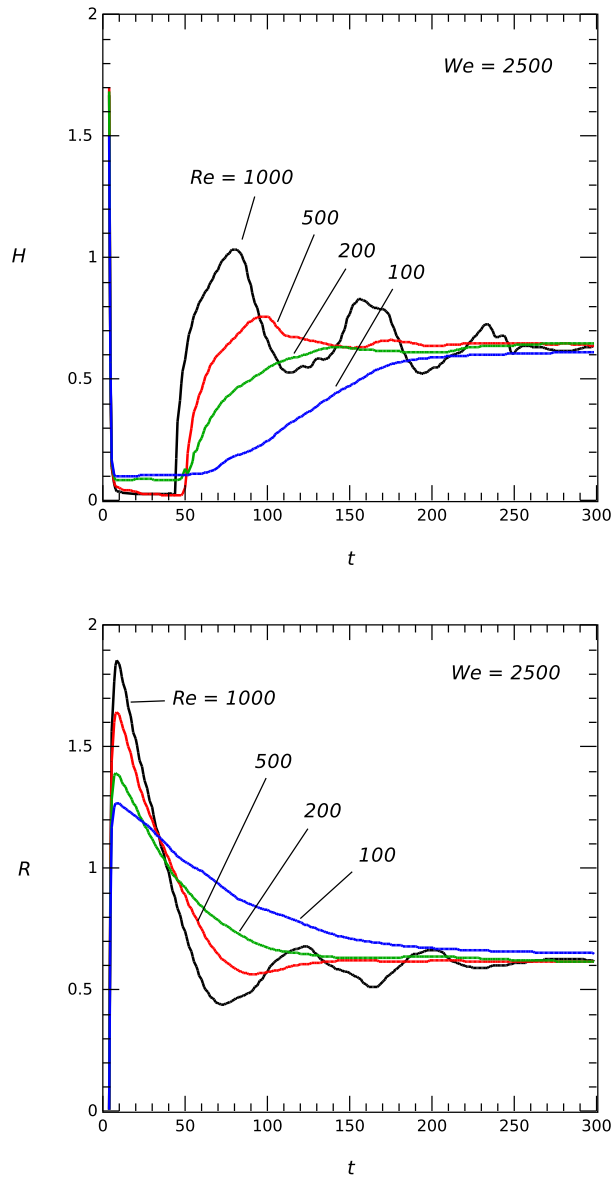


Figure 5. Plots of the center height H (z -value at $r = 0$ of free surface) and contact radius R (r -value at $z = 0$ of free surface) in units of d versus time in units of d/U ($= 0.05 \mu\text{s}$), for droplets of $d = 5 \mu\text{m}$, $\rho_d = 2000 \text{ kg m}^{-3}$, $\sigma = 0.04 \text{ N m}^{-1}$, with $\mu_d = 1 \text{ cp}$ ($Re = 1000$ and $Ca = 2.5$), 2 cp ($Re = 500$ and $Ca = 5$), 5 cp ($Re = 200$ and $Ca = 12.5$), and 10 cp ($Re = 100$ and $Ca = 25$), impacting solid surface at $U = 100 \text{ m/s}$ for contact angle $\theta_0 = 90^\circ$.

begin to recede, which is sometimes called the relaxation phase because the receding contact line now is moving at a relatively much lower speed (as shown in figure 3 and $R(t)$ in figure 5). After the relaxation phase, the impact kinetic energy is almost dissipated by the viscous effect, and the droplet will go through a slow lengthy ‘wetting equilibrium’ phase (e.g., $R(t) \propto t^{1/10}$ according to Tanner, 1979) toward the capillary equilibrium determined by the static contact angle.

Among many variables involved in droplet impact dynamics, the maximum spread

Table 1. Comparison of the present computed values of the maximum spread factor ξ with that predicted by (7) at $We = 2500$, for droplets of $d = 5 \mu\text{m}$, $\rho_d = 2000 \text{ kg m}^{-3}$, $\sigma = 0.04 \text{ N m}^{-1}$ with various values of viscosity μ_d , when impacting solid surface at $U = 100 \text{ m/s}$ for contact angle $\theta_0 = 90^\circ$ (with $\theta_A = 95^\circ$ and $\theta_R = 85^\circ$).

μ_d (cp)	Re	Ca	Oh	ξ	Eq. (7)	Eq. (8)
1	1000	2.5	0.05	3.696	3.676	3.870
2	500	5	0.1	3.281	3.276	3.382
5	200	12.5	0.25	2.796	2.814	2.827
10	100	25	0.5	2.462	2.508	2.468
100	10	250	5	1.714	1.711	1.567

factor, characterizing the maximum value of contact diameter normalized with the diameter of the undeformed droplet before impaction, has often been considered in the literature for describing the impaction dynamics as well as for comparing results. The maximum spread factor can be brought to bear on various practical applications such as inkjet printing, spray coating, pesticide application, etc. where the actual droplet coverage area directly corresponds to maximum spreading due to rapid solidification at contact line, liquid absorption into porous substrate, contact line pinning on a textured surface, and so on so forth. According to an empirical correlation by Scheller and Bousfield (1995), the maximum spread factor $\xi \equiv 2R_{max}$ may be expressed as (cf. Yarin, 2006)

$$\xi = 0.61 \times (Re^2 Oh)^{0.166} . \quad (7)$$

Another semiempirical relation was proposed by Roisman (2009) which, out of numerous possibilities, is presented here in a modified form as

$$\xi = Re^{1/5} - 0.35Re^{2/5}/\sqrt{We} , \quad (8)$$

with the original factors 0.87 and 0.40 replaced here by 1.0 and 0.35 for a better match to the values of present computational results.

A comparison of (7) and (8) with the present results is given in table 1 (for a constant $We = 2500$), which shows remarkably good agreements. As reasonably accurate as they may seem though, neither (7) nor (8) explicitly accounts for the contact angle effect, which was somehow justified by experiments (cf. Scheller and Bousfield, 1995). According to Rioboo et al. (2002), immediately after the droplet touches the substrate (and throughout most part of the spreading phase) the contact line motion is controlled by the dominant kinetic energy, irrespective of the physical properties of the liquid and solid such as the contact angle. Thus, contact angle may not be expected to have significant effect on the dynamics of spreading following the droplet impact and the value of maximum contact radius R at the end of spreading.

To test the validity of (7) and (8) for contact angles other than $\theta_0 = 90^\circ$, computations of cases for $\theta_0 = 45^\circ$ (with $\theta_A = 50^\circ$ and $\theta_R = 40^\circ$) while other parameters remain unchanged from those in table 1) are also performed. The results show that $\xi = 3.827$ for $\mu_d = 1$

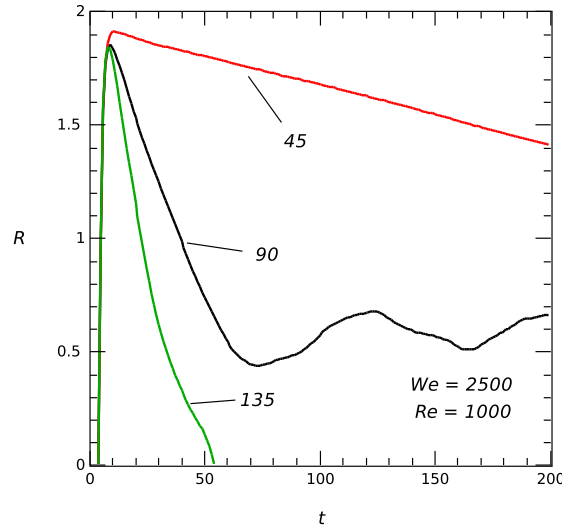


Figure 6. Plot of contact radius R , as in figure 5, with $\mu_d = 1$ cp ($Re = 1000$ and $Ca = 2.5$), but for contact angle $\theta_0 = 45^\circ$, 90° , and 135° , as labeled.

cp ($Re = 1000$), 3.396 for 2 cp ($Re = 500$), 2.849 for 5 cp ($Re = 200$), 2.484 for 10 cp ($Re = 100$), and 1.724 for 100 cp ($Re = 10$), with a spreading time $\approx 6.5 \times d/U$ ($= 0.325 \mu\text{s}$) which is about $0.1 \mu\text{s}$ longer than the case of $\theta_0 = 90^\circ$ for droplets of $d = 5 \mu\text{m}$ at $U = 100$ m/s, Results for $\theta_0 = 135^\circ$ (with $\theta_A = 140^\circ$ and $\theta_R = 130^\circ$) show that $\xi = 3.624$ for $\mu_d = 1$ cp ($Re = 1000$), 3.231 for 2 cp ($Re = 500$), 2.782 for 5 cp ($Re = 200$), 2.448 for 10 cp ($Re = 100$), and 1.705 for 100 cp ($Re = 10$), with a spreading time $\approx 3.5 \times d/U$ ($= 0.175 \mu\text{s}$). Hence, the computed values of ξ (at $We = 2500$) are indeed insensitive to the contact angle variations, as consistent with the experimental findings of Scheller and Bousfield (1995).

However, the contact angle may drastically influence the dynamics of free surface deformation after the completion of spreading phase (as described by Rioboo et al., 2002). Figure 6 shows that a droplet with contact angle $\theta_0 = 45^\circ$ (at $Re = 1000$ and $Ca = 2.5$) recedes very slowly in contrast to the case of $\theta_0 = 90^\circ$ with considerable oscillations after receding, while the droplet with $\theta_0 = 135^\circ$ recedes rapidly with great momentum such that it bounces off the solid surface (around $t = 51$).

Physically, bouncing can occur when kinetic energy of impact remains sufficiently large in the receding phase if the viscous dissipation effect is relatively weak such that the shrinking lamella contact line virtually disappears near the impact point (Yarin, 2006). Figure 7 shows the snapshots of such free surface shape evolution from spreading to receding-bouncing, with streamlines being also displayed to illustrate external gas flow field interaction with the free surface deformation at different stages. Clearly, the liquid droplet impact dynamics can influence the external gas flow significantly. In view of the gas flow streamline configuration, the droplet, having about the same velocity as the surrounding gas at $t = 0$, moves ahead the decelerating gas due to its inertia as it approaches the substrate at $t = 3$. The fast moving liquid phase tends to drag nearby gas at an increased velocity during the droplet spreading phase, e.g., at $t = 5$. Toward the end of droplet spreading phase, e.g., at $t = 8$, as the liquid

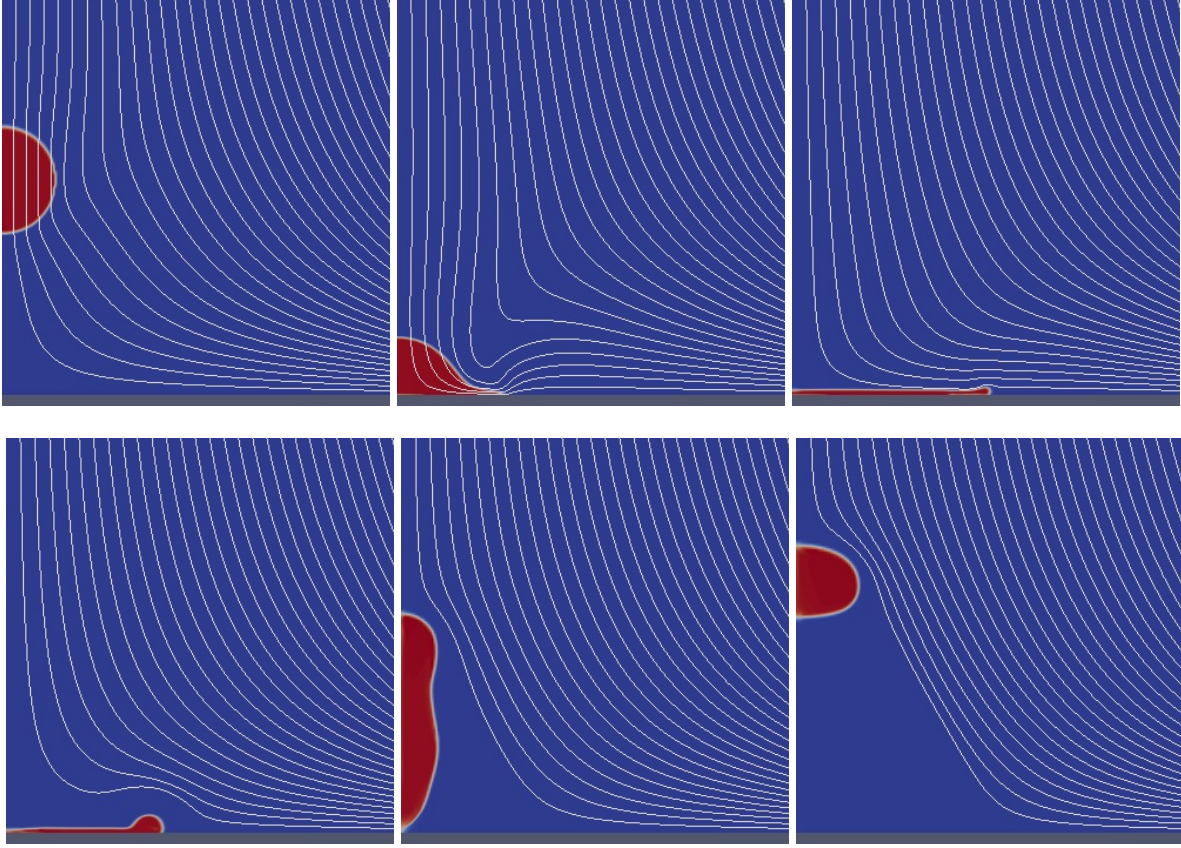


Figure 7. Streamlines associated with a droplet impaction at $Re = 1000$ and $Ca = 2.5$ ($We = 2500$ and $Oh = 0.05$, as in figure 2), but for contact angle $\theta_0 = 135^\circ$ ($\theta_A = 140^\circ$, $\theta_R = 130^\circ$) for spreading at $t = 3, 5, 8$ in the upper row, and receding to bouncing at $t = 15, 51, \text{ and } 80$ in the lower row.

phase motion decreases the gas phase around free surface recovers its natural impinging jet type of flow. During the relatively slow receding process, e.g., at $t = 15$ a somewhat stagnant zone in the gas phase develops near the free surface. As the droplet leaving the substrate during bouncing, a low velocity wake appear behind it, e.g, at $t = 51$ and 80 . The bouncing droplet is expected to experience a gas flow resistance that tends to push it back toward the substrate. Eventually, the bouncing droplet will come back to reattach to the substrate due to the external gas flow of an impinging jet.

An examination of the effect of liquid viscosity μ_d for a droplet with contact angle $\theta_0 = 135^\circ$ indicates that the dynamics after spreading is also controlled by the value of Reynolds number Re . Figure 8 shows that receding momentum decreases with increasing μ_d (namely, reducing Re), and bouncing would not occur when $Re = 250$ (for R never reaches zero before recoving to a spreading phase again). At $Re = 333$ the droplet detaches from the substrate around $t = 93$, but reattaches to the substrate around $t = 143$ for lack of bouncing momentum. Reducing Re tends to increase the time from the droplet impact to its detaching from substrate, if bouncing occurs. For example, a droplet with $Re = 1000$ impacts the substrate at $t = 4.5$ and detaches from the substrate at $t \approx 53$, with $Re = 500$ at $t \approx 63$,

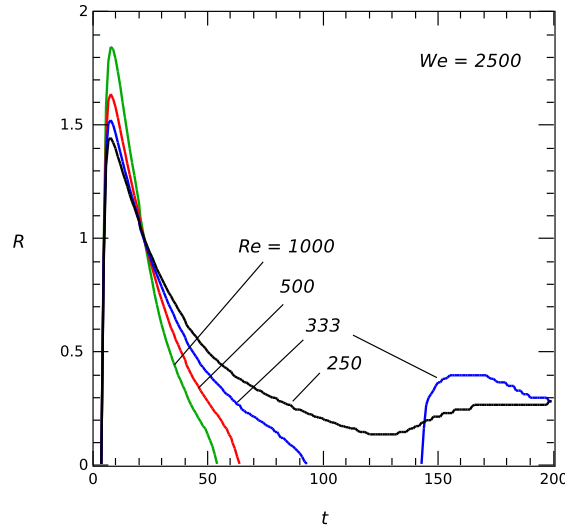


Figure 8. Plot of contact radius R , as in figure 6, with $\mu_d = 1$ cp ($Re = 1000$ and $Ca = 2.5$), $\mu_d = 2$ cp ($Re = 500$ and $Ca = 5.0$), $\mu_d = 3$ cp ($Re = 333$ and $Ca = 7.5$), and $\mu_d = 4$ cp ($Re = 250$ and $Ca = 10$), for contact angle $\theta_0 = 135^\circ$.

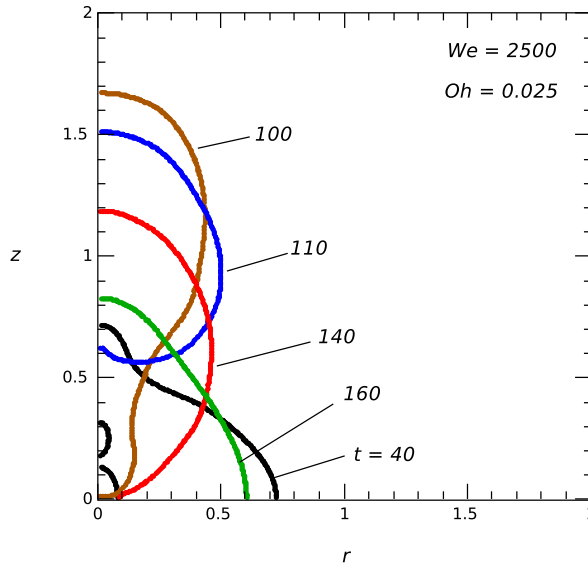


Figure 9. Detaching and reattaching: as in figure 2 but for $\rho_d = 4000$ kg m $^{-3}$ and surface tension $\sigma = 0.08$ N m $^{-1}$ ($Re = 2000$ and $Ca = 1.25$, or $We = 2500$ and $Oh = 0.025$) with $\theta_0 = 90^\circ$ at $t = 40, 100, 110, 140,$ and 160 .

and with $Re = 333$ at $t \approx 96$. As expected, liquid viscosity has an effect of retarding the free surface flow during receding-bouncing.

If a droplet of $d = 5$ μm with viscosity $\mu_d = 1$ cp has density $\rho_d = 4000$ kg m $^{-3}$ and surface tension $\sigma = 0.08$ N m $^{-1}$, the values of Re and Ca for $U = 100$ m/s become 2000 and 1.25, which lead to $We = 2500$ and $Oh = 0.025$. The computed maximum spread factor is $\xi = 4.177$, while (7) and (8) predict 4.124 and 4.4267, respectively. This may be considered

as an extreme case for relatively weak droplet viscosity effect compared to the inertial and surface tension effects directly relevant to Aerosol Jet[®] droplet deposition. Because of the reduced viscous effect, enhanced free surface deformations can be observed. Figure 9 shows a phenomenon of detaching and reattaching, after a droplet impact for $Re = 2000$ and $Ca = 1.25$ (or $We = 2500$ and $Oh = 0.025$) with $\theta_0 = 90^\circ$. Entrapped bubbles can be seen to form during the receding phase, as indicated in the free surface profile at $t = 40$. The center height H reaches its peak value 1.779 at $t = 83$. The contact radius R shrinks to zero at $t = 106$ corresponding to the time for complete detachment of the droplet from substrate, when the free surface pinches off at the end of a tail formed at the droplet bottom (cf. the free surface profile at $t = 100$). The tip of such tail moves rapidly upward into the bulk of the droplet, due to the action of surface tension, leaving a deep dimple on the droplet bottom at $t = 110$. While moving downward and oscillating with a considerable amplitude, the bottom of the detached droplet reattaches the substrate at $t = 140$. Thereafter, the attached droplet exhibits significant oscillatory motions with even larger amplitudes than that shown in figure 4, as a consequence of relatively stronger effects of fluid inertia and surface tension.

3.2. Cases of $We = 100$

If the droplet of $d = 5 \mu\text{m}$, $\rho_d = 2000 \text{ kg m}^{-3}$, $\mu_d = 1 \text{ cp}$, and $\sigma = 0.04 \text{ N m}^{-1}$ has an impact velocity of 20 m/s, the values of Re and Ca become 200 and 0.5 such that $We = 100$ and $Oh = 0.05$. The spreading time for $We = 100$ is around $t = 2.0$, corresponding to a dimensional time of $\approx 2.0 \times d/U$ ($= 0.5 \mu\text{s}$ for $d = 5 \mu\text{m}$ and $U = 20 \text{ m/s}$), which seems to be consistent with the experimental findings of drop impact scaling time $t \times d/U \propto We^{-0.25}$ by Antonini et al. (2012),

The effect of increasing liquid viscosity μ_d on dynamics of a droplet of $d = 5 \mu\text{m}$, $\rho_d = 2000 \text{ kg m}^{-3}$, and $\sigma = 0.04 \text{ N m}^{-1}$ with an impact velocity of 20 m/s is shown in figure 10 for the center height H and contact radius R versus time. It is interesting to note that the curves in figure 10 are quite similar to those in figure 5 corresponding to the same values of Oh , despite more than an order of magnitude reduction of We . Because there is a factor of 5 difference in the reference time scale d/U (due to a factor of 5 reduction of U), the normalized time interval $(0, 60)$ for t in figure 10 has the same dimensional time interval $(0, 15\mu\text{s})$ as $(0, 300)$ for t in figure 5. This is expected in view of the fact that the impact velocity U only provides the initial free surface deformation that sets the droplet into free oscillatory motion, the characteristics of which is usually determined by fluid density ρ_d , droplet size d , and surface tension σ (Landau and Lifshitz, 1959). Noteworthy here is that the Ohnesorge number Oh ($\equiv \mu_d/\sqrt{\rho_d\sigma d}$) is independent of U , unlike Re , Ca , and We . The fluid viscosity contained in Oh is responsible for the decay of oscillation amplitude, whereas ρ_d , d , and σ are the key ingredients for capillary driven oscillations. Similar to the case of $We = 2500$, the oscillatory motion seems to also diminish for $Oh > 0.25$ at $We = 100$.

Similar to that shown in figure 5, the center height H decrease with t after impaction. But the lamella at $We = 100$ is thicker (with larger H_{min}) than that corresponding to the same value of Oh at $We = 2500$. For example, the values of H_{min} are reached as 0.0353 at

Table 2. Comparison of the present computed values of the maximum spread factor ξ with that predicted by (7) at $We = 100$, for droplets of $d = 5 \mu\text{m}$, $\rho_d = 2000 \text{ kg m}^{-3}$, $\sigma = 0.04 \text{ N m}^{-1}$ with various values of viscosity μ_d , when impacting solid surface at $U = 20 \text{ m/s}$ for contact angle $\theta_0 = 90^\circ$ (with $\theta_A = 95^\circ$ and $\theta_R = 85^\circ$).

μ_d (cp)	Re	Ca	Oh	ξ	Eq. (7)	Eq. (8)
1	200	0.5	0.05	2.415	2.154	2.594
2	100	1	0.1	2.149	1.920	2.291
5	40	2.5	0.25	1.819	1.649	1.938
10	20	5	0.5	1.606	1.470	1.705
100	2	50	5	1.143	1.003	1.103

$t = 9.6$ for $Re = 200$, 0.1097 at $t = 7.8$ for $Re = 100$, 0.1940 at $t = 6.8$ for $Re = 40$, and 0.2881 at $t = 6.2$ for $Re = 20$ and 500 , respectively. While the oscillatory characteristics following the spreading phase appear independent of the impact velocity U (and the value of We), the thickness of the spreading lamella as well as the maximum spread factor are strongly influenced by the value of We .

The computed values of maximum spread factor $\xi = 2R_{max}$ for $We = 100$ at various Re corresponding to various values of μ_d for droplets of $d = 5 \mu\text{m}$, $\rho_d = 2000 \text{ kg m}^{-3}$, $\sigma = 0.04 \text{ N m}^{-1}$ with an impact velocity of $U = 20 \text{ m/s}$ are given in table 2, along with that predicted by (7) and (8). Again, the agreement between the present computations and either (7) or (8) is quite reasonable. It should be noted that the value of ξ for the case of $\mu_d = 100 \text{ cp}$ ($Re = 2$) is actually smaller than that at capillary equilibrium for 90° contact angle (i.e., 1.26). The ξ in this case may not be literally regarded as the ‘‘maximum spread factor’’. What is given here is actually the peak value of the spread factor $2R$ marking the end of spreading phase. In this case, the contact radius R decreases slightly for a while from its peak value in the relaxation phase, and then slowly increases toward the capillary equilibrium value 0.63 .

To check the validity of (7) and (8) for contact angles other than $\theta_0 = 90^\circ$, computations of cases for $\theta_0 = 45^\circ$ and 135° (while other parameters remain unchanged from those in table 2) are also performed. The results show that $\xi = 2.647$ and 2.272 for $\mu_d = 1 \text{ cp}$ ($Re = 200$), 2.293 and 2.064 for 2 cp ($Re = 100$), 1.905 and 1.796 for 5 cp ($Re = 40$), 1.632 and 1.596 for 10 cp ($Re = 20$), and 1.143 and 1.143 for 100 cp ($Re = 2$). A trend seems to exist indicating a diminishing difference between the values ξ for $\theta_0 = 45^\circ$ and 135° with increasing Oh which is a measure of relative strength of the viscosity effect. In general, the computed values of ξ (at $We = 100$) are insensitive to the contact angle variations, as consistent with the experimental findings of Scheller and Bousfield (1995) and reasoning of Rioboo et al. (2002) for insignificant influence of contact angle to ξ .

However, the dynamics of free surface flow after initial spreading can be quite sensitive to the contact angle when $We = 100$, similar to that shown for $We = 2500$. A droplet with $\theta_0 = 45^\circ$ recedes very slowly whereas the contact line of that with $\theta_0 = 135^\circ$ moves rapidly during receding such that bouncing can occur. Noteworthy here is that the same droplet of $d = 5 \mu\text{m}$, $\rho_d = 2000 \text{ kg m}^{-3}$, $\sigma = 0.04 \text{ N m}^{-1}$ with viscosity $\mu_d = 5$, ($Oh = 0.25$) and

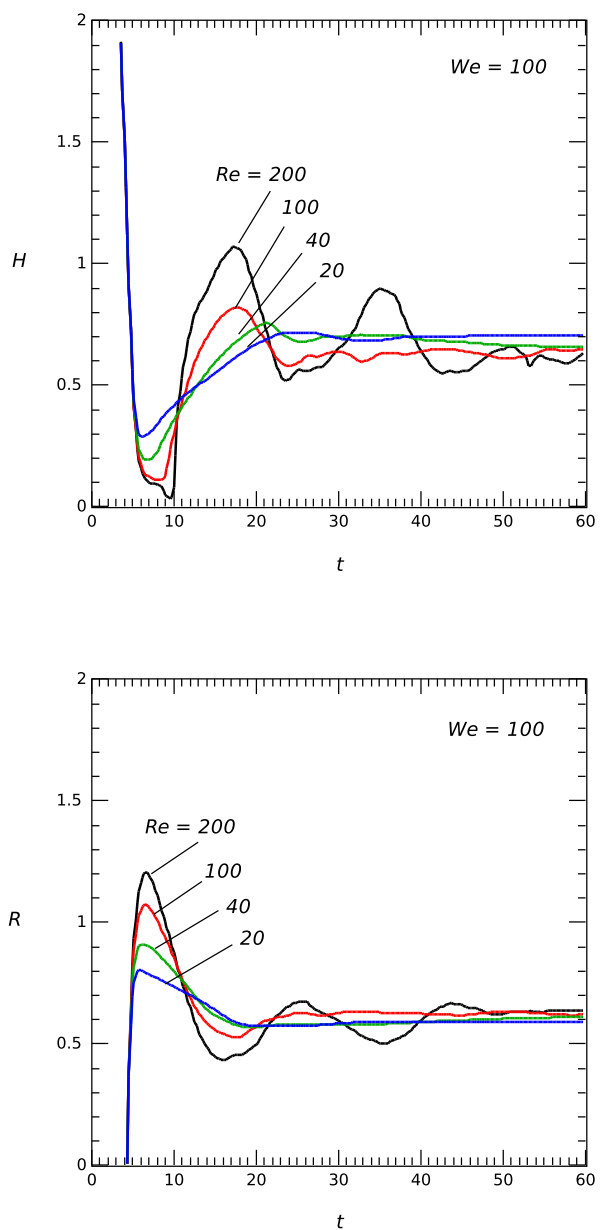


Figure 10. Plots of the center height H and contact radius R in units of d versus time in units of d/U ($= 0.25 \mu\text{s}$), for droplets of $d = 5 \mu\text{m}$, $\rho_d = 2000 \text{ kg m}^{-3}$, $\sigma = 0.04 \text{ N m}^{-1}$, with $\mu_d = 1 \text{ cp}$ ($Re = 200$ and $Ca = 0.5$), 2 cp ($Re = 100$ and $Ca = 1$), 5 cp ($Re = 40$ and $Ca = 2.5$), and 10 cp ($Re = 20$ and $Ca = 5$), impacting solid surface at $U = 20 \text{ m/s}$ for contact angle $\theta_0 = 90^\circ$.

$\theta_0 = 135^\circ$ would bounce (i.e., detach) from substrate at $t = 26.8$ for lower impact velocity $U = 20$ m/s ($We = 100$) but remain attached to the substrate at $U = 100$ m/s ($We = 2500$, as indicated in figure 8). This appears to be consistent with the trend shown by Durickovic and Varland (2005) for water drop impact on a solid surface and by Law (2015) in a general description of impact dynamics of droplets that bouncing is expected at lower We , due to large free surface deformation along the squeezing gas gap with reduced impact inertia, while merging-absorption at higher We , due to sufficient impact inertia.

3.3. Cases of $We = 5$

For a relatively small droplet of $d = 1 \mu\text{m}$, $\rho_d = 1000 \text{ kg m}^{-3}$, $\mu_d = 1 \text{ cp}$, and $\sigma = 0.08 \text{ N m}^{-1}$ with an impact velocity of 20 m/s, the values of Re and Ca become 20 and 0.25 such that $We = 5$ and $Oh = 0.1118$. For the same values of Re and Ca (as well as We and Oh), we can compute solutions with the same (dimensional) OpenFOAM mesh for $d = 5 \mu\text{m}$, $\rho_d = 200 \text{ kg m}^{-3}$, $\mu_d = 1 \text{ cp}$, and $\sigma = 0.08 \text{ N m}^{-1}$ with an impact velocity of 20 m/s.

Figure 11 shows the variations of droplet surface profile with time for $We = 5$ and $Oh = 0.1118$. In contrast to figures 2—4 for $We = 2500$ and $Oh = 0.05$, the droplet surface in figure 11 does not form a commonly observed thin lamella with a bulged rim at the end of spreading phase ($t = 5.6$) due to lack of impact momentum. The maximum contact radius at $t = 5.6$ is 0.6995 while the center height reaches its minimum value of 0.4571, (which is much larger than 0.0266 in subsection 3.1 for $We = 2500$ and $Oh = 0.05$). Following the end of spreading phase, the contact radius recedes and then oscillates with rather small amplitudes. Increasing liquid viscosity μ_d , for a droplet of $d = 5 \mu\text{m}$, $\rho_d = 200 \text{ kg m}^{-3}$, and $\sigma = 0.08 \text{ N m}^{-1}$ with an impact velocity of 20 m/s, further reduces the magnitude of dynamics of free surface variations. The value of contact radius R could not even reach its capillary equilibrium value during the spreading phase for $\mu_d \geq 5 \text{ cp}$ ($Oh \geq 0.5590$); rather it slowly creeps toward 0.63 in the lengthy wetting equilibrium phase. However, even for the case of $\mu_d = 10$ ($Oh = 1.1180$) the center height H still exhibits noticeable oscillatory motions, because of weaker viscous damping effect in the thick lamella away from the solid wall.

If the liquid viscosity μ_d is increased to 10 cp ($Re = 2$ and $Ca = 2.5$), the receding and oscillation phase disappears, with the contact radius R increase with time t monotonically as shown in figure 12. However, there still seems to be a spreading phase corresponding to a rapid increase of R , i.e., with a relatively large dR/dt , followed by a relaxation phase with diminishing dR/dt toward capillary equilibrium $R \approx 0.63$. Because there are no local extrema for a peak of R , the end of spreading phase cannot be clearly defined. The fact that the profile at $t = 10.0$ with a monotonically increasing contact radius R has a center height H slightly greater than that at $t = 5.6$ around the end of spreading phase, indicating an oscillating free surface shape.

Table 3 shows the computed values of maximum spread factor $\xi = 2R_{max}$ for $We = 5$ at various Re corresponding to various values of μ_d for droplets of $d = 5 \mu\text{m}$, $\rho_d = 200 \text{ kg m}^{-3}$, $\sigma = 0.08 \text{ N m}^{-1}$ with an impact velocity of $U = 20$ m/s, along with that predicted by (7) and

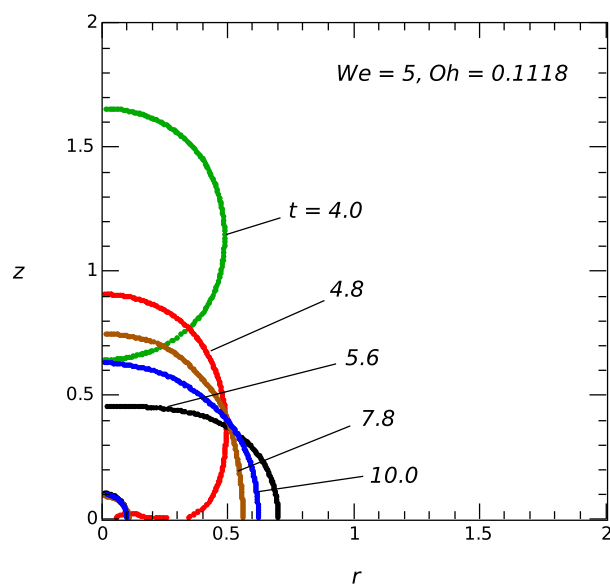


Figure 11. As in figure 2 but for $\rho_d = 200 \text{ kg m}^{-3}$, $\mu_d = 1 \text{ cp}$, and $\sigma = 0.08 \text{ N m}^{-1}$ ($Re = 20$ and $Ca = 0.25$, or $We = 5$ and $Oh = 0.1118$) with $\theta_0 = 90^\circ$ at $t = 4.0, 4.8, 5.6, 7.8,$ and 10.0 .

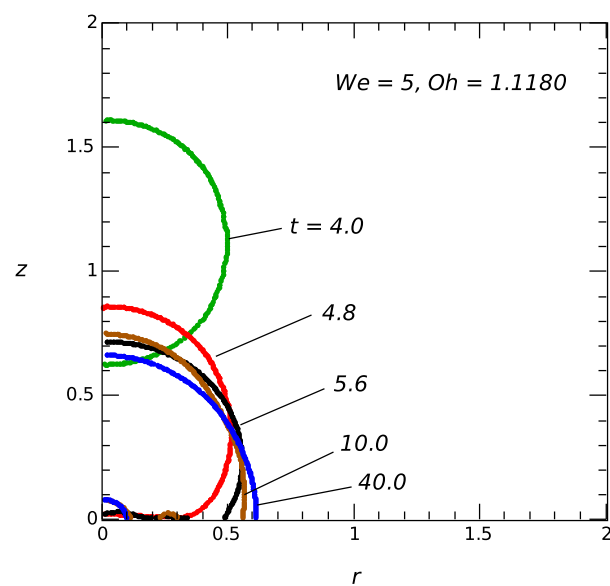


Figure 12. As in figure 11 but for $\mu_d = 10 \text{ cp}$ ($Re = 2$ and $Ca = 2.5$, or $We = 5$ and $Oh = 1.1180$) at $t = 4.0, 4.8, 5.6, 10.0,$ and 40.0 .

Table 3. Comparison of the present computed values of the maximum spread factor ξ with that predicted by (7) at $We = 5$, for droplets of $d = 5 \mu\text{m}$, $\rho_d = 200 \text{ kg m}^{-3}$, (or equivalently $d = 1 \mu\text{m}$, $\rho_d = 1000 \text{ kg m}^{-3}$), $\sigma = 0.08 \text{ N m}^{-1}$ with various values of viscosity μ_d , when impacting solid surface at $U = 20 \text{ m/s}$ for contact angle $\theta_0 = 90^\circ$ (with $\theta_A = 95^\circ$ and $\theta_R = 85^\circ$).

μ_d (cp)	Re	Ca	Oh	ξ	Eq. (7)	Eq. (8)
1	20	0.25	0.1118	1.399	1.146	1.302
2	10	0.5	0.2236	1.285	1.022	1.192
5	4	1.25	0.5590	~ 1.120	0.878	1.047
10	2	2.5	1.1180	~ 1.050	0.782	0.942
100	0.2	25	11.1803	~ 0.835	0.534	0.643

(8). Again, the agreement between the present computations and either (7) or especially (8) is still reasonable. For the cases of $Re \leq 4$, the value of ξ is taken as the (normalized) contact diameter at the end of spreading phase rather than literally the maximum contact diameter. However, the end of spreading phase may not be clearly defined. In the case of $Re = 4$, a local extremum (or peak) of R exists; so such a local peak value of R is used as R_{max} for calculating ξ . But in the cases of $Re = 2$ and 0.2 , $R(t)$ increases monotonically without local extrema; the end of spreading phase can only be estimated based on the slope change. Therefore, the estimated values of ξ in table 3 are marked by an approximation sign (\sim).

If computations are performed for cases of $We = 5$ with θ_0 other than 90° (while other parameters remain unchanged from those in table 3), the results for the value of ξ seems to still be reasonably close to those for $\theta_0 = 90^\circ$, especially when the liquid viscosity μ_d is large. For example, with $\theta_0 = 135^\circ$ for $\mu_d = 5 \text{ cp}$ ($Re = 4$) and 10 cp ($Re = 2$) a local extremum appears with the peak value of contact radius $R_{max} = 0.503$ or $\xi = 1.006$ and $R_{max} = 0.469$ or $\xi = 0.938$, which are especially close to predicted values of 1.047 and 0.942 by (8). The value of ξ remains the same at 0.835 for the case of $\mu_d = 100 \text{ cp}$ at $\theta_0 = 135^\circ$. But for $\mu_d = 1 \text{ cp}$ ($Re = 20$) and $\mu_d = 2 \text{ cp}$ ($Re = 10$), the values of R_{max} for $\theta_0 = 135^\circ$ become 0.5985 or $\xi = 1.1970$ and 0.5558 or $\xi = 1.1116$, which are more than 10% off the corresponding values in table 3 for $\theta_0 = 90^\circ$. Similarly with $\theta_0 = 45^\circ$ and $\mu_d = 1$ ($Ca = 0.25$), the computed $\xi = 1.656$ is $\sim 18\%$ off 1.399 in Table 3. Hence, the effect of contact angle θ_0 on maximum spread factor ξ seems to become more noticeable at small values of We (e.g., $We < 10$), especially when μ_d (or Ca) is small.

As shown with the cases of $We = 2500$ and 100 , bouncing tends to occur for droplet impact onto a hydrophobic surface. However, for $We = 5$ with $\theta_0 = 135^\circ$, droplet bouncing after impact only happens when the liquid viscosity is very low, e.g., $\mu_d = 1 \text{ cp}$ ($Re = 20$). Thus, the simple trend of bouncing at relatively smaller We (e.g., Durickovic and Varland, 2005; Law, 2015) may not be general enough to cover all cases. For example, the obvious effect of liquid viscosity on the likelihood of bouncing illustrated in figure 8 cannot be accounted for with the Weber number alone.

4. Discussion

Generally speaking, (7) and (8) seems to describe the maximum spread factor ξ fairly accurately over a wide range of parameters for high-speed microdroplet impact. with (8) being slightly more favorable in comparison with the present computational results. Noteworthy here is that different empirical, semiempirical formulas were many as proposed in the literature, with substantial discrepancies among each other (as illustrated by Perelaer et al., 2009; Ravi et al., 2010; Visser et al., 2012, 2015). After comparing with several of the available formulas, (7) and (8) are selected because the agreement between them and with the presently computed results appear to be quite consistent across the ranges of parameters relevant to the Aerosol Jet[®] technology. However, neither (7) nor (8) explicitly accounts for the contact angle effect, which tends to become more noticeable with reduced We and small Ca (e.g., $We = 5$ and $Ca < 1$). Unlike (7) and (8), the maximum spread factor formula derived by Pasandideh-Fard et al. (1996) based on energy balance actually contains the contact angle θ_0 as

$$\xi = \sqrt{\frac{12 + We}{3(1 - \cos \theta_0) + 4\sqrt{CaWe}}} \quad (9)$$

Despite its considerable discrepancy from the computed ξ values in the present work, (9) indeed suggests that the contact angle effect should diminish when the value of $Ca \times We$ becomes close to 100 or greater. It also qualitatively predicts the trend of decreasing contact angle effect on ξ with increasing Ca (or viscosity μ_d) as consistent with the present results. In view of the general accuracy of (8) and reasonable account for the trend of contact angle effect with (9), a straightforward combination of the two yields

$$\xi = \left(Re^{1/5} - 0.35 \frac{Re^{2/5}}{\sqrt{We}} \right) \sqrt{\frac{3 + 4\sqrt{CaWe}}{3(1 - \cos \theta_0) + 4\sqrt{CaWe}}} \quad (10)$$

For example, in the case of a droplet with $d = 1 \mu\text{m}$, $\rho_d = 1000 \text{ kg m}^{-3}$, $\sigma = 0.08 \text{ N m}^{-1}$, and $\mu_d = 1 \text{ cp}$ impacting the substrate at $U = 20 \text{ m/s}$ (i.e., $We = 5$ and $Ca = 0.25$) and $\theta_0 = 135^\circ$, the computed $\xi = 1.197$ and that calculated with (10) is 1.149 whereas with (8) 1.302. If μ_d is increased to 2 cp (i.e., $We = 5$ and $Ca = 0.5$), the computed $\xi = 1.112$ and that calculated with (10) is 1.076 whereas with (8) 1.192. With $\theta_0 = 45^\circ$ for $\mu_d = 1$ and 2 cp ($Ca = 0.25$ and 0.5), the computed ξ are 1.656 and 1.379 while that predicted by (10) are 1.539 and 1.356, much improved from 1.302 and 1.192 by (8). Thus, (10) can be a useful formula with improved accuracy for the range of parameters of practical interest to applications with the Aerosol Jet[®] direct-write technology.

While the maximum spread factor ξ provides a practically useful correlation between the Feret diameter of deposited individual droplet on a dry substrate and the diameter of corresponding droplet before impact, other dynamic outcomes of droplet impact can be relevant to Aerosol Jet[®] ink deposition, too. Although not computed with the present axisymmetric model, the splashing phenomenon usually observed in droplet impact with large We and Re is also of great importance to Aerosol Jet[®] printing for being a possible source of undesirable oversprays and uncontrolled satellites. Historically, the first study of splashing

after droplet impact was carried out by Worthington (1876). Splashing of large milk and mercury droplets onto smooth glass plates was observed and the corresponding fingering patterns were sketched, with the number of fingers increasing with both droplet size and fall height being noted. Several investigations on surface roughness effect on splashing behavior suggested that splashing at atmospheric pressure only occurs when

$$K \equiv \frac{We}{Oh^{2/5}} > K_s \quad \text{with} \quad K_s = 649 + \frac{3.76}{R_a^{0.63}} \quad , \quad (11)$$

where R_a denotes the nondimensional roughness parameter in units of d (Stow and Hadfield, 1981; Mundo et al., 1995; Cossali et al., 1997; Yarin, 2006). Thus, $K_s \rightarrow 649$ as $R_a \rightarrow \infty$ for a very rough surface, whereas K_s increases to infinity as $R_a \rightarrow 0$ for an extremely smooth surface. However, other forms for splashing criteria had also been proposed in the literature (e.g., Moreira et al., 2010; Mandre and Brenner, 2012; Stevens, 2014), but little agreement had been shown among different proposed criteria which often contradict one another (Visser et al., 2015). While careful examining the validity of each proposed criterion is out of scope of the present work, (11) may be used as a tentative reference for a brief discussion here.

In the case of Aerosol Jet[®] ink droplets with $d = 5 \mu\text{m}$, $R_a = 0.1$ (which leads to $K_s = 665$, only slightly greater than 649) corresponds to a roughness length scale ($0.5 \mu\text{m}$) around the wavelengths of visible light which is usually considered as a fairly smooth surface with most of realistic substrate surfaces. For cases with $U = 100 \text{ m/s}$ ($We = 2500$), as those in table 1, the values of K are all exceeding 649 (or 665), ranging from 1313 for $Re = 10$ to 8286 for $Re = 1000$. Thus, when operating at a very high jet speed (e.g., $U = 100 \text{ m/s}$) under atmospheric pressure, the Aerosol Jet[®] ink droplets of $d = 5 \mu\text{m}$ are expected to disintegrate as a consequence of splashing after impacting the substrate. If the ink droplet d is reduced to $2 \mu\text{m}$ with $\mu_d = 100 \text{ cp}$ at the same U , the value of K can become 437 (< 649). Even for an ink droplet of $d = 1 \mu\text{m}$ with $\mu_d = 5 \text{ cp}$ (for $\rho_d = 2000 \text{ kg m}^{-3}$ and $U = 100 \text{ m/s}$), the value of K is 631, barely below the reference splashing threshold value 649. Thus, to avoid ink droplet splashing upon deposition in Aerosol Jet[®] printing with high-speed jet, it is preferable to keep the droplet size small and viscosity high (which may be accomplished by enabling effective in-flight mist solvent evaporation).

5. Concluding remarks

In view of the challenges with required high spatial and temporal resolutions for experimentally analyzing the ink droplet deposition behavior during Aerosol Jet[®] printing (with microdroplets of diameters from 1 to $5 \mu\text{m}$ and impact velocity from 20 to 100 m/s), numerical solutions for high-speed microdroplet impact onto a smooth solid surface are computed in the present work using the *interFoam* VoF solver of the OpenFOAM[®] CFD package. For simplicity and computational efficiency, the free-surface fluid dynamics problem is assumed to be axisymmetric with incompressible flow. The computed results illustrate droplet impact dynamics with lamella shape evolution throughout the spreading, receding-relaxation, and wetting equilibrium phases, consistent with what have been observed and described in various previous studies. This fact agrees with the conclusions of Visser et al.

(2015) that the basic droplet impact behavior is scale-invariant; in other words, experiments with larger droplets at the same nondimensional parameter values should be able to describe the phenomena with much smaller droplets. When the droplet viscosity is relatively low, significant oscillations in the free-surface flow can be observed. But the free surface oscillatory motion seems to diminish as the droplet viscosity μ_d becomes relatively high. The border line between periodic free surface oscillations and aperiodic creeping to capillary equilibrium free surface shape after impact spreading appears at Ohnesorge number Oh ($\equiv \mu_d/\sqrt{\rho_d\sigma d}$) about 0.25. Understanding the controlling factors for free surface oscillations can be important for Aerosol Jet[®] ink formulation and process recipe development.

The computed results show that substrate surface properties such as the contact angle can drastically influence the dynamics of free surface deformation after the spreading phase. For example, droplet bouncing (i.e., rebound) is prompted with large contact angles at solid surface (i.e., hydrophobic surface, consistent with findings reported in the literature, cf. Rioboo et al., 2001; Durickovic and Varland, 2005), but its likelihood can be reduced by increasing the droplet viscosity due to enhanced kinetic energy dissipation. At some intermediate viscosity values, reattachment of the bouncing droplet to the solid surface can be observed within a short time. When using a high-speed jet flow to direct the ink droplet deposition in Aerosol Jet[®] printing, droplet bouncing after impact on substrate is generally undesirable for causing unintended ink placement such as “satellite”, “overspray”, etc.

Special attention has been paid to the value of maximum spread factor ξ , which can be accurately determined from the numerical solutions. Given substantial discrepancies among different correlations by many authors in the literature, comparisons with the presently computed ξ have been performed to construct a useful formula with reasonable accuracy. For the range of parameters of practical interest to the Aerosol Jet[®] printing, the values of computed ξ agree quite well with the empirical correlation of Scheller and Bousfield (1995) based mostly on experimental data and the semiempirical relation proposed by Roisman (2009) based on an analytical theory for inertia dominated situations (with a slight modification of the coefficient values). Majority of the computed cases show insignificant variations of ξ with changes of contact angle θ_0 , as expected when dynamics in the spreading phase is dominated by inertial effect. The weak dependence of ξ on contact angle θ_0 , especially becoming more noticeable at relatively small Ca and We , can be accounted for with a straightforward combination of the formula of Pasandideh-Fard et al. (1996) and that of Roisman (2009). The resulting maximum spread factor formula can be used for first-order evaluations of deposited ink droplet size during Aerosol Jet[®] technology development.

Acknowledgment

The author would like to thank John Lees for encouragement and guidance, and Dr. Mike Renn for insightful discussion.

References

- Antonini, C., Amirfazli, A., and Marengo, M., 2012 Drop impact and wettability: From hydrophilic to superhydrophobic surfaces, *Phys. Fluids* 24, 102104
- Attane, P., Girard, F., and Morin, V., 2007 An energy balance approach of the dynamics of drop impact on a solid surfaces. *Phys. Fluids* 19, 012101
- Berberovic, E., Van Hinsber, N. P., Jakirlic, S., Roisman, I. V., Tropea, C., 2009. Drop impact onto a liquid layer of finite thickness: Dynamics of the cavity evolution. *Phys. Rev. E* 79(3), 036306.
- Bussmann, M., Mostaghimi, J., Chandra, S. 1999 On a three-dimensional volume tracking model of droplet impact. *Phys. Fluids* 11(6), 1406–1417
- Bussmann, M., Chandra, S., Mostaghimi, J. 2000 Modeling the splash of a droplet impacting a solid surface. *Phys. Fluids* 12(12), 3121–3132
- Chandra, S. and Avedisian, C. T. 1991 On the collision of a droplet with a solid surface. *Proc. R. Soc. London* A432, 13–41
- Christenson, K.K., Paulsen, J.A., Renn, M.J., McDonald, K., and Bourassa, J. 2011 Direct printing of circuit boards using Aerosol Jet[®]. *Proc. NIP 27 Digital Fabric.*, 433–436
- Cossali, G. E., Coghe, A., and Marengo, M., 1997 The impact of a single drop on a wetted sold surface. *Exp. Fluids* 22, 463–472
- Deshpande, S. S., Lakshman, A., and Trujillo, M. F., 2012 Evaluating the performance of the two-phase flow solver interFoam. *Comput. Sci. Discov.* 5, 04016
- Dinc, M. and Gray, D. D., 2012 Drop impact on a wet surface: computational investigation of gravity and drop shape. *Advance in Fluid Mechanics and Heat & Mass Transfer* (ISBN: 978-1-61804-114-2), pp 374–379
- Durickovic, B. and Varland, K., 2005 Between bouncing and splashing: water drops on a solid surface. *Applied Mathematics thesis*, USA; University of Arizona
- Feng, J. Q. 2010 A deformable liquid drop falling through a quiescent gas at terminal velocity. *J. Fluid Mech.* 658, 438–462
- Feng, J. Q. 2015 Sessile drop deformations under an impinging jet. *Theor. Comput. Fluid Dyn.* 29, 277–290
- Ford, R. E. and Furmidge, C. G. L. 1967 Impact and spreading of spray drops on foliar surfaces. *Wetting, Soc. Chem. Industry Monograph*, 417–432
- Foot, G. B. 1974 The water drop rebound problem: dynamics of collision. *J. Atmos. Sci.* 32, 390–402
- German, G., and Bertola, V., 2009 Review of drop impact models and validation with high-viscosity Newtonian fluids. *Atom. Sprays* 19(8), 787–807
- Gopala, V. R. and van Wachem, B. G. M., 2008 Volume of fluid method for immiscible-fluid and free-surface flows. *Chem. Eng. J.* 141(1), 204–221
- Gupta, A. and Kumar, R., 2010 Droplet impingement and breakup on a dry surface. *Comput. Fluids* 39, 1696–1703
- Healy, W. M., Hartely, J. G., Abdel-Khalik, S. I. 1996 Comparison between theoretical models and experimental data for the spreading of liquid droplets impacting a solid surface. *Int. J. Heat Mass Transfer* 39, 3079–3082
- Hedges, M., King, B. and Renn, M. 2007 Direct writing for advanced electronics packaging. www.onboard-technology.com/pdf_giugno2007/060706.pdf
- Hoang, D. A., van Steijn, V., Portela, L. M., Kreutzer, M. T., and Kleijn, C. R. 2013 Benchmark numerical simulations of segmented two-phase flows in microchannels using the volume of fluid method. *Comput. Fluids* 86, 28–36
- Kahn, B.E. 2007 The M³D aerosol jet system, an alternative to inkjet printing for printed electronics, *Organic and Printed Electronics*, 1, 14–17
- Landau, L. D. and Lifshitz, E. M. 1959 *Fluid Mechanics*. Addison-Wesley
- Law, C. K. 2015 Impact dynamics of droplets and jets. *ICLASS2015, 13th Int. Conf. Liquid Atom. Spray Syst.* Tainan, Taiwan
- Linder, N., Roisman, I. V., Marschall, H., and Tropea, C. 2013 Numerical simulations of pinning droplets. *ILASS–Europe 2013, 25th Europ. Conf. Liquid Atom. Spray Syst.* Chania, Greece
- Mandre, S. and Brenner, M. P., 2012 The mechanism of a splash on a dry solid surface. *J. Fluid Mech.* 690,

148–172

- Moreira, A. L. N., Moita, A. S., and Panao, M. R., 2010 Advances and challenges in explaining fuel spray impingement: how much of single droplet impact research is useful? *Prog. Energy Combust. Sci.* 36, 554–580
- Morgan, G. C. J., 2013 Application of the interFoam VoF code to coastal wave/structure interaction. PhD thesis: University of Bath
- Mundo, C., Sommerfeld, M., and Tropea, C., 1995 Droplet-wall collisions: experimental studies of the deformation and breakup process. *Int. J. Multiphase Flow* 21, 151–173
- Pasandideh-Fard, M., Qiao, Y. M., Chandra, S. and Mostaghimi, J. 1996 Capillary effects during droplet impact on a solid surface. *Phys. Fluids* 8, 650–659
- Paulsen, J. A., Renn, M., Christenson, K., and Plourde, R. 2012 Printing conformal electronics on 3D structures with Aerosol Jet technology. In Future of Instrumentation International Workshop (FIIW) doi: 10.1109/FIIW.2012.6378343
- Perelaer, J., Smith, P. J., van den Bosch, E., van Grootel, S. S. C., Ketelaars, P. H. J. M., and Schubert, U. S. 2009 The spreading of inkjet-printed droplets with varying polymer molar mass on a dry solid substrate. *Macromol. Chem. Phys.* 210, 495–502
- Ravi, V., Jog, M. A., and Manglik, R. M. 2010 Effects of interfacial and viscous properties of liquids on drop spread dynamics. ILASS2010-142, 22nd Ann. Conf. Liquid Atom. Spray Syst. Cincinnati, OH
- Rein, M. 1993 Phenomena of liquid drop impact on solid and liquid surfaces. *Fluid Dyn. Res.* 12, 61–93
- Renn, M. J. 2006 Direct WriteTM system. US Patent 7,108,894 B2
- Renn, M. J. 2007 Direct WriteTM system. US Patent 7,270,844 B2
- Renn, M. J., King, B. H., Essien, M., Marquez, G. J., Giridharan, M. G., and Sheu, J.-C. 2009 Apparatuses and methods for maskless mesoscale material deposition. US Patent 7,485,345 B2
- Renn, M., Essien, M., King, B. H., and Paulsen, J. A. 2010 Aerodynamic jetting of aerosolized fluids for fabrication of passive structures. US Patent 7,674,671 B2
- Rioboo, R., Tropea, C., and Marengo, M. 2001 Outcomes from a drop impact on solid surfaces. *Atomiz. Sprays* 11, 155–165
- Rioboo, R., Marengo, M., and Tropea, C. 2002 Time evolution of liquid drop impact onto solid, dry surface. *Exp. Fluids* 33, 112–124
- Roisman, I. V. 2009 Inertia dominated drop collisions. II. An analytical solution of the Navier-Stokes equations for a spreading viscous film. *Phys. Fluids* 21, 052104
- Rusche, H. 2002 Computational fluid dynamics of dispersed two-phase flows at high phase fractions. PhD thesis, University of London / Imperial College
- Saha, A. A. and Mitra, S. K. 2009 Effect of dynamic contact angle in a volume of fluid (VoF) model for a microfluidic capillary flow. *J. Colloid Interf. Sci.* 339, 461–480
- Scheller, B. L. and Bousfield, D. W. 1995 Newtonian drop impact with a solid surface. *AIChE J.* 41, 1357–1367
- Sikalo, S., Marengo, M., Tropea, C., Ganic, E. N. 2002 Analysis of impact of droplet on horizontal surfaces. *Exp. Therm. Fluid Sci.* 25, 503–510
- Stevens, C. S. 2014 Scaling of the splash threshold for low viscosity fluids. *Europhys. Lett.* 106, 24001
- Stow, C. D. and Hadfield, M. G. 1981 An experimental investigation of fluid flow resulting from the impact of a water drop with an unyielding dry surface. *Proc. R. Soc. Lond.* A373, 419–441
- Tanner, L. H. 1979 The spreading of silicone oil drops on solid surfaces. *J. Phys. D* 12, 1473–1484
- Toivakka, M. 2003 Numerical investigation of droplet impact spreading in spray coating of paper. Proceedings of TAPPI 8th Advanced Coating Fundamentals Symposium
- Ubbink, H. 2002 Computational Fluid Dynamics of Dispersed Two-Phase Flows at High Phase Fractions. PhD Thesis, Imperial College of Science, Technology and Medicine, London
- Visser, C. W., Tragawa, Y., Sun, C., and Lohse, D. 2012 Microdroplet impact at very high velocity. *Soft Matter* 8, 10732
- Visser, C. W., Frommhold, P. E., Wildeman, S., Mettin, R. Lohse, D., and Sun, C. 2015 Dynamics of high-speed micro-drop impact: numerical simulations and experiments at frame-to-frame times below 100ns. *Soft Matter* 11, 1708-1722

- Worthington, A. M. 1876 On the forms assumed by drops of liquids falling vertically on a horizontal plate. *Proc. R. Soc. Lond.* 25, 261–271
- Yarin, A. L. 2006 Drop impact dynamics: splashing, spreading, receding, bouncing... *Ann. Rev. Fluid Mech.* 38, 159–192
- Zollmer, V., Muller, M., Renn, M., Busse, M., Wirth, I., Godlinski, D., and Kardos, M. 2006 Printing with aerosols: A maskless deposition technique allows high definition printing of a variety of functional materials, *Euro. Coating J.*, 07-08, 46–55